CHAPTER 17

BORON-NITRIDE-CONTAINING NANOTUBES

NASREEN G. CHOPRA and ALEX ZETTL

17.1 INTRODUCTION

Graphite is a layered material in which each sheet is a hexagonal grid of carbon atoms covalently bonded to each other in the plane with van der Waals bonds between layers. The covalent bond is one of the strongest in nature while the van der Waals bond is weak; thus, planes may easily slide relative to each other. A nanotube can be described mathematically as a long thin strip, cut out of a single atomic plane of material, rolled to form a cylinder with a diameter of nanometer scale and a length on the order of micrometers. Carbon nanotubes were first discovered by Iijima in 1991 [1] while performing transmission electron microscopy (TEM) on a fullerene sample taken from the chamber where C_{60} [2] is produced. The discovery has led to extensive interest in many fields due to the versatility and potential applications of these nanostructures. Experimental observations of carbon nanotubes demonstrate that tubes may be single-walled or multiwalled structures, sometimes with over 50 walls. Multiwalled tubes are hollow, seamless cylinders that are concentrically organized such that the spacing between walls approximately equals the graphitic interplanar distance. Perhaps the most unique feature of these nanostructures is their high aspect ratio. Inner diameters of nanotubes range from 7 Å to about 4 nm, while their lengths are typically several micrometers, even up to several hundred micrometers.

Nanotubes have been a rich source of inspiration for theorists. Indeed, much of the excitement about nanotubes stems from the prediction of their interesting electrical and mechanical properties. Calculations show that the electrical behavior of nanotubes is integrally related to the specific geometry of the tube structure [3]; that is, a carbon nanotube can be semiconducting or metallic, depending on its radius and chirality. Empirical formulation of the rigidity of

Fullerenes: Chemistry, Physics, and Technology, Edited by Karl M. Kadish and Rodney S. Ruoff.
0-471-29089-0 Copyright © 2000 John Wiley & Sons, Inc.

nanotubes finds nanotubes to be extremely strong in the axial direction with predicted elastic moduli exceeding 1 TPa [4] for these structures.

Theorists have also predicted the existence of tubes made from other layered materials such as boron nitride [5], BC_2N [6], and BC_3 [7]. All of these materials are hexagonal networks of atoms, which imitate the planar sp^2 bonding in graphite. Band structure calculations predict unique, and equally interesting, electrical properties for each of these novel tubes. The mechanical properties of $B_xC_yN_z$ nanotubes are again expected to be exceptional.

This chapter summarizes theoretical and experimental investigations of boron-nitride-containing nanotubes, including pure BN nanotubes and nanotubes of stoichiometries BC_2N and BC_3. Section 17.2 compares the crystal structures of graphite, BN, BC_2N, and BC_3. In the case of BC_2N and BC_3, only the single-sheet structure is considered. Section 17.3 investigates the theoretical band structure of graphite and pure BN, both in bulk and nanotube form. Further theoretical predictions for the electronic properties of boron-nitride-containing nanotubes are presented in Section 17.4. Section 17.5 introduces experimental synthesis and characterization of $B_xC_yN_z$ nanotubes and proposes possible nanotube growth mechanisms. The mechanical (elastic) properties of pure BN nanotubes are described in Section 17.6. It is found that a BN nanotube is the stiffest insulating fiber known, most likely due to the inherent strength of the BN bond and the high degree of crystallinity of BN nanotubes. The last section summarizes BN, BC_2N, and BC_3 nanotube properties and comments on additional $B_xC_yN_z$ nanostructures, including carbon/BN nano "coaxial cables."

17.2 COMPARISON OF CRYSTAL STRUCTURES OF GRAPHITE, BN, BC_2N, AND BC_3

The crystal structures of graphite, BN, BC_2N, and BC_3 are quite similar. They are all hexagonal layered structures, with ABAB packing being the most common arrangement of the layers. The crystal structure is best described by schematics of the ideal structures.

17.2.1 Graphite

See Figure 17.1.

17.2.2 BN

See Figure 17.2.

17.2.3 BC_2N

See Figures 17.3 (Type I) and 17.4 (Type II).

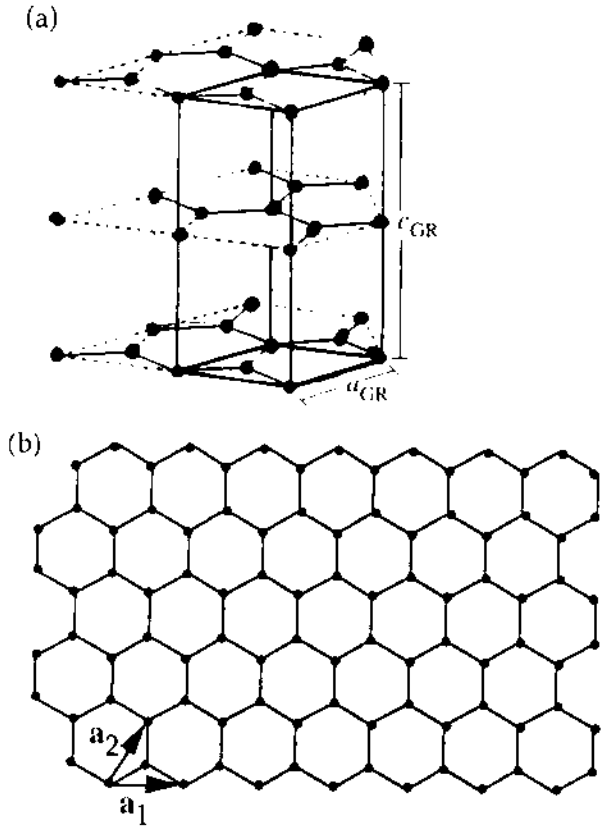

Figure 17.1 Crystal structure of graphite. (a) Unit cell has lattice constant of $a_{GR} = 2.46\,\text{Å}$ [8], which corresponds to the second-nearest-neighbor distance, and the interplanar spacing is $c_{GR}/2 = 3.36\,\text{Å}$. (b) Graphite is a hexagonal sheet with carbon atoms at each vertex. The bond length is $d_{C\text{-}C} = 1.42\,\text{Å}$. Lattice translation vectors are shown and have magnitudes equal to $|\vec{\mathbf{a}}_1| = |\vec{\mathbf{a}}_2| = a_{GR}$. Due to the homogeneity of the material, this sheet structure has inversion symmetry.

17.2.4 BC_3

See Figure 17.5.

17.3 THEORETICAL BAND STRUCTURE OF CARBON AND BN NANOTUBES

The band structure for carbon nanotubes is derived primarily from the band structure of graphite. Thus, a brief discussion of the unique features of the graphite band structure precedes that of nanotubes. Emphasis is placed on a pictorial description rather than involved calculations.

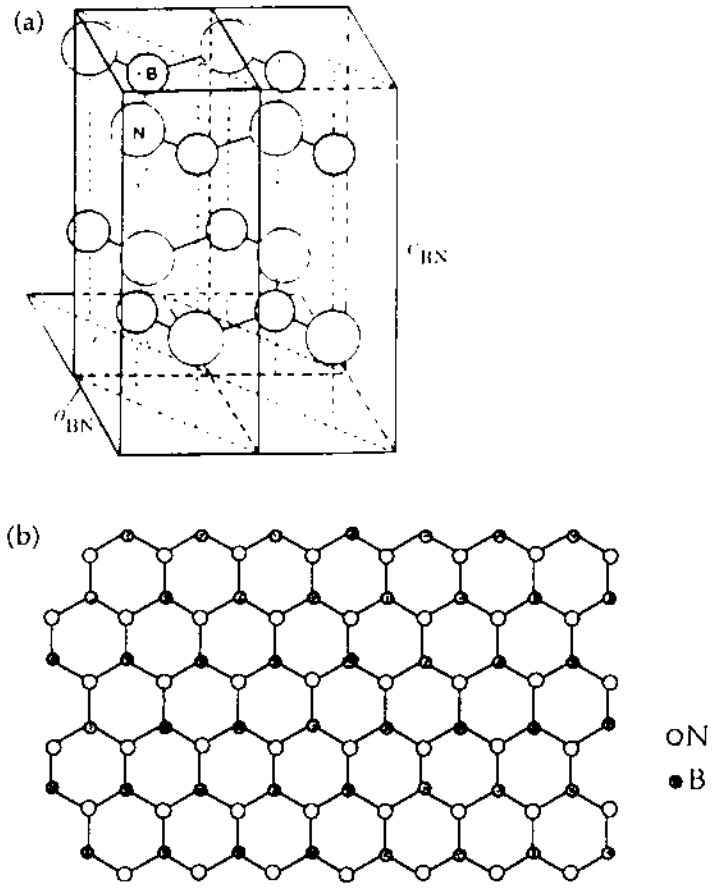

Figure 17.2 Crystal structure of BN. (a) Unit cell has lattice constant of $a_{BN} = 2.50$ Å, which corresponds to the second-nearest-neighbor distance, and the interplanar spacing is $c_{BN}/2 = 3.33$ Å [9]. (b) BN is a hexagonal sheet with boron atoms surrounded by nitrogen atoms and vice versa. The bond length is $d_{B\ N} = 1.44$ Å. Lattice translation vectors are defined similar to the graphite sheet with $|\vec{a_1}| = |\vec{a_2}| = a_{BN}$. Because of the dissimilar B and N atoms, this sheet arrangement does not have inversion symmetry.

17.3.1 Band Structure of Graphite

There are two common orientations of the two-dimensional hexagonal lattice of graphite. The lattice (grid) may be oriented such that a side of the hexagonal unit is parallel to either (1) the x axis or (2) the y axis. If the repeat unit in real space is the hexagon oriented as shown in Figure 17.6a (i.e., parallel to the y axis), the Brillouin zone (BZ) of the sheet consists of hexagons rotated[1] by 90° as displayed in Figure 17.6b (parallel to the x axis). The central point ($\vec{k} = 0$) is

[1] This rotation is a consequence of the mathematical formalism used when transforming from real space to reciprocal space (see Chapter 2 in *Introduction to Solid State Physics* by Kittel).

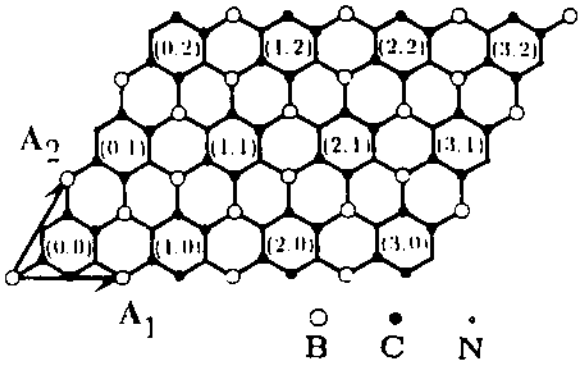

Figure 17.3 Structure of BC_2N (Type I) sheet. The unit cell is about twice that of either graphite or BN as seen from the lattice translation vectors, $\vec{A}_1$ and $\vec{A}_2$. Bond lengths determined from theoretical work are the following: $d_{C\text{-}C} = 1.42$ Å, $d_{B\text{-}C} = 1.55$ Å, $d_{B\text{-}N} = 1.45$ Å, and $d_{C\text{-}N} = 1.32$ Å [6]. The distance between layers is determined from experiment to be 3.35 Å for this material [10]. Note that for this particular arrangement of B, C, and N atoms, the sheet has inversion symmetry.

Γ while the corner point is labeled **K** (all the corner points are equivalent). The unique feature of graphite is that it has a Fermi *point*, instead of a surface, because the valence and conduction bands meet exactly at the **K** points as is apparent in the graphite band structure plot of Figure 17.6c.

17.3.2 Band Structure of Carbon Tubes

Since a tube may be formed mathematically by cutting a strip from a graphite sheet and rolling it into a cylinder, the two-dimensional sheet becomes a one-

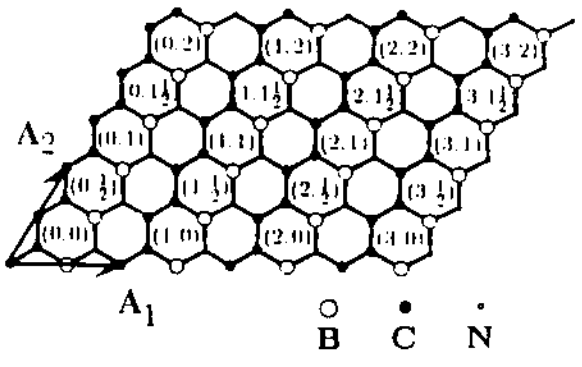

Figure 17.4 Structure of BC_2N (Type II) sheet. Lattice translation vectors, $\vec{A}_1$ and $\vec{A}_2$, are identical to those shown for the Type I material (Fig. 17.3). Bond lengths determined from theoretical work are the same as for Type I [6]. The distance between layers is determined from experiment to be 3.35 Å [10]. Note that for this particular arrangement of B, C, and N atoms, the sheet does not have inversion symmetry.

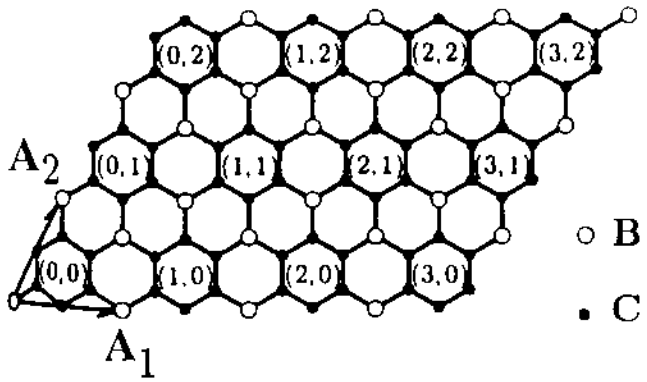

Figure 17.5 Structure of BC_3 sheet. Lattice translation vectors, $\vec{A}_1$ and $\vec{A}_2$, are similar to those shown for BC_2N material. Bond lengths determined from theoretical work are the following: $d_{C-C} = 1.42$ Å and $d_{C-B} = 1.55$ Å [7]. The distance between layers is determined from experiment to be 3.35 Å [10]. The unique arrangement of B and C atoms causes this heterogeneous sheet to have inversion symmetry.

dimensional tube structure. The curvature induces σ-π hybridization, which introduces some sp^3 character into the planar sp^2 nature of the carbon bonds. This hybridization, however, only significantly affects small tubes; thus, for the most part, the energy bands of nanotubes may be derived explicitly from the graphite band structure. Due to the high aspect ratio of nanotubes, the axial dimension is still considered infinite but the periodic boundary conditions around the tube circumference now constrain the allowed k values. The *sheet* wave vector $\vec{k}$ will be included if it satisfies the condition of single-valuedness of

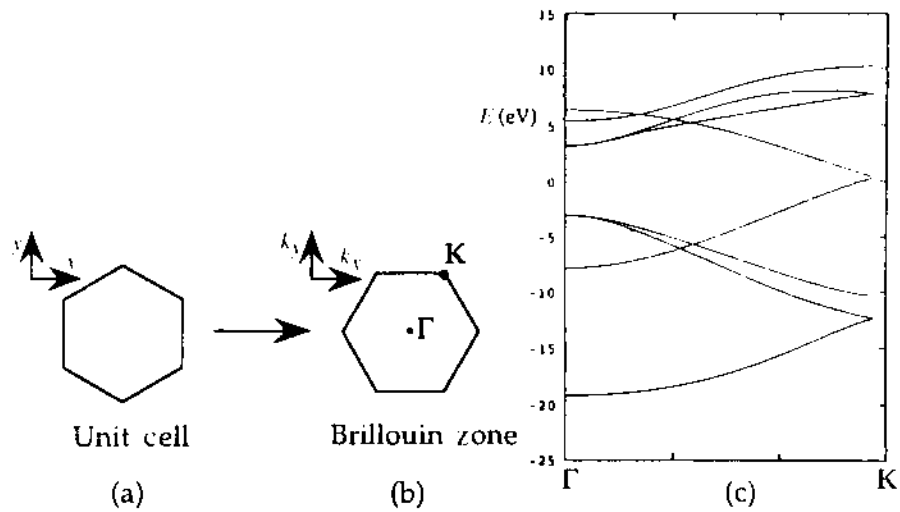

Figure 17.6 Band structure of graphite. (a) Unit cell of graphite. (b) BZ of graphite. (c) Band structure of graphite.

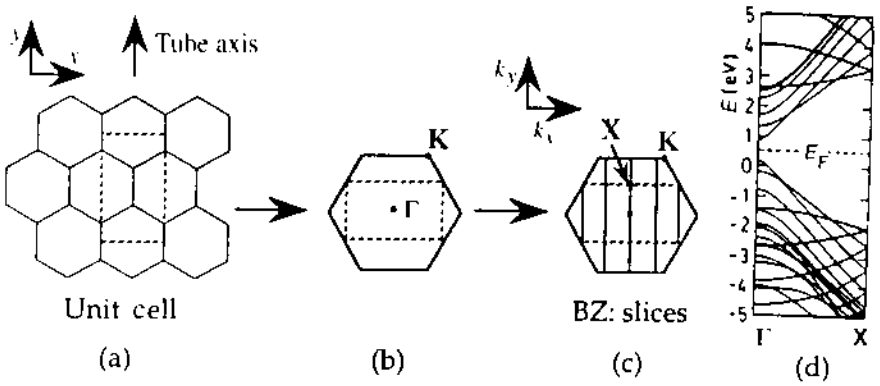

Figure 17.7 Band structure of zigzag carbon nanotube. (a) Tubular unit cell. (b) BZ of zigzag tube relative to graphite BZ. (c) Tubes have BZ lines as opposed to areas. These give the allowed k values for the (4, 0) tube. (d) Band structure for (13, 0) tube [3].

the *tube* wave function:

$$\vec{\mathbf{C}} \cdot \vec{\mathbf{k}} = 2\pi \mathbf{J}, \quad \mathbf{J} = 0, 1, 2, 3, \ldots \tag{17.1}$$

where $\vec{\mathbf{C}}$ is the circumference vector of the tube. This constraint manifests itself as allowed *lines* in the reciprocal lattice instead of an area. The construction of the band structure of nanotubes is best illustrated by example.

17.3.2.1 Zigzag Tubes Figure 17.7 describes the formation of the band structure for an $(n, 0)$ tube, which is referred to as a zigzag tube. The repeat unit for this tube along the tube axis is shown in Figure 17.7a. Because this unit cell is bigger than the hexagonal unit cell of graphite, the BZ is smaller. Figure 17.7b shows the BZ of a zigzag tube relative to that of graphite. k_y, corresponding to the direction along the tube axis, can take on a continuum of values but k_x is discretized. Now, the allowed k values depend on the particular circumference vector $\vec{\mathbf{C}}$. Let us take the (4, 0) tube specifically. The allowed k values then lie along the lines drawn in Figure 17.7c and the tube bands are given by the corresponding graphite bands for those k values. Since the allowed points in this particular case do not include the **K** point, the tube is semiconducting. From symmetry, the bands can be folded onto each other so that complete band information may be conveyed between the Γ and **X** points. As labeled in Figure 17.7c, the **X** refers to the edge of the BZ in the k_y direction; thus, the coordinates are determined directly from the size of the tubular unit cell. In this case $\mathbf{X} = \pi/\sqrt{3}a_{\mathrm{GR}}$ for all $(n, 0)$ tubes. The $(n, 0)$ carbon nanotubes, which are semiconducting, have direct gaps because the tube band may be folded onto the $k_x = 0$ line from symmetry arguments. Continuing this kind of construction for other values of n gives the following results: Tubes that have $n = 3J$, where $J = 1, 2, 3, \ldots$, are narrow-gap semiconductors and the rest are semiconductors with gaps ranging up to 1.25 eV. Figure 17.7d shows the band structure of the (13, 0) tube.

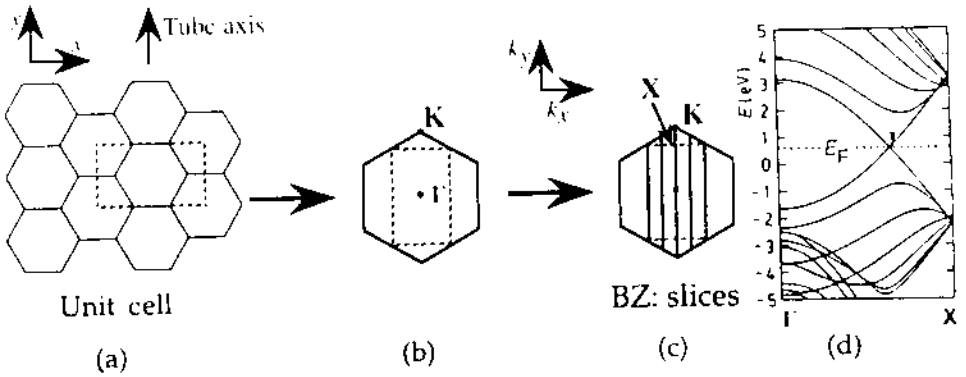

Figure 17.8 Band structure of armchair carbon nanotube. (a) Tubular unit cell. (b) BZ of armchair tube relative to graphite BZ. (c) BZ of the (2, 2) tube. (d) Band structure for (6, 6) tube [3].

17.3.2.2 Armchair Tubes As another example, let us take the case of an (n, n) armchair tube. Figure 17.8 is analogous to Figure 17.7. Note the repeat unit has now rotated by 90° from the previous case. This time, $\mathbf{X} = \pi/a_{GR}$ in accordance with the armchair tubular unit cell, and the **K** point is always included because $k = 0$ is always allowed. Thus, all armchair chirality tubes are metallic. In fact, these have the distinction of being the only tubes calculated to be metallic. The band structure of the (6, 6) tube is shown in Figure 17.8c.

Simular analyses may be done for the other (n_1, n_2) carbon nanotubes. The BZ in each case will be oriented slightly differently with the angle of rotation reflecting the helicity designated by the particular $\vec{C}$.

17.3.3 BN Band Structure

Planar hexagonal BN has a lattice almost identical to that of graphite. Thus, the BZ of the BN sheets and tubes may be constructed in a similar fashion. For comparison, the band structures of a BN sheet and the (4, 4) BN nanotube are shown in Figure 17.9. Note that the conduction and valence bands are separated by a gap, which arises from the asymmetry in the crystal potential due to the heterogeneous lattice of B and N atoms.

17.4 PREDICTED PROPERTIES OF BN, BC_2N, AND BC_3 NANOTUBES

17.4.1 Theoretical Predictions of BN Nanotubes

17.4.1.1 Nanotubular Structure As discussed earlier, hexagonal boron nitride (BN) is a layered material with approximately the same lattice param-

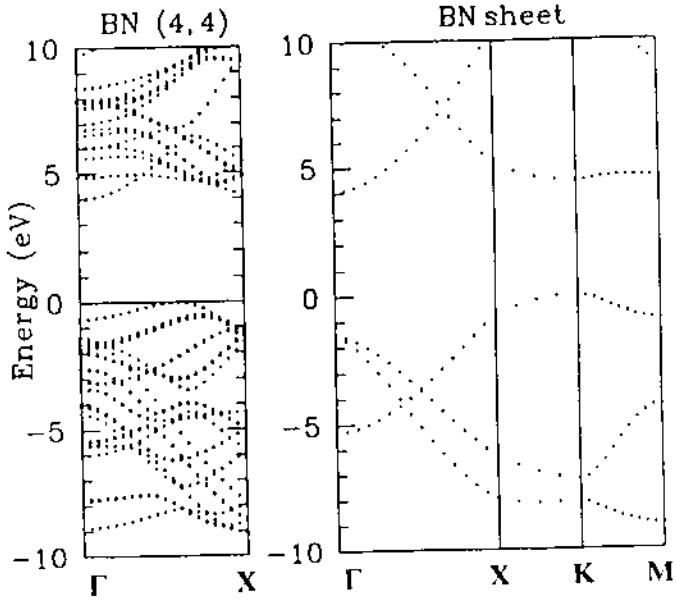

Figure 17.9 Band structure of (a) BN sheet and (b) a BN (4, 4) nanotube [11].

eters as graphite. The main difference, of course, is that while in graphite each vertex of the hexagon is occupied by a carbon atom, in BN a boron atom is surrounded by three nitrogen atoms or vice versa. The bonding between the boron and nitrogen atoms is also sp^2-like in nature, but the asymmetry in the crystal potential, arising from the dissimilar atoms, causes bulk hexagonal BN to be an insulator with a gap of 5.8 eV [12]. Authors of a tight-binding calculation originally proposed that nanotubes might also be formed from hexagonal BN [5]. Theoretical formulation of a BN tube is identical to the carbon case described earlier, where a strip is cut out of a hexagonal sheet and rolled to form a tube. Thus, BN tubes may also be formed with a variety of diameters and chiralities depending on the circumference vector $\vec{C}$.

Total energy calculation results of the strain energy needed to form a tube of a given diameter are shown in Figure 17.10 [11]. The closed circles represent the energy needed to form a BN tube relative to a sheet of hexagonal BN, while the open circles indicate the energy of a carbon nanotube relative to graphite. Clearly, the tubes are higher energy structures, but compared to their respective sheet material, BN nanotubes are energetically even more favorable than carbon ones and therefore likely to form.

17.4.1.2 Electrical and Mechanical Properties Local density approximation (LDA) and quasi-particle band structure calculations predict BN tubes to be semiconducting with a gap of roughly 4–5.5 eV *independent* of tube diameter, chirality, and number of tube walls [11]. This uniformity in the calculated electronic properties of BN nanotubes contrasts sharply with the heter-

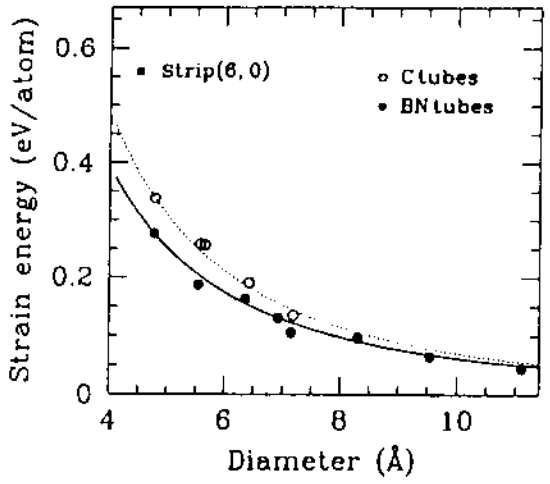

Figure 17.10 Strain energy versus diameter for the formation of BN and carbon nanotubes relative to their sheet structures. Closed and open circles indicate the energy for BN and carbon nanotubes, respectively. (Courtesy of X. Blase.)

ogeneity of carbon tubes and suggests that BN tubes may present significant advantages from an applications point of view. Details of the tube band structure show that the lowest lying state is a nearly free-electron-like state, which has a maximum charge density about 2 Å interior to the tube wall. Thus, if the BN tubes were doped with, say, carbon, the resulting metallic tube would carry a cylinder of charge internally along its length.

Theoretical calculations of the elastic properties predict that BN nanotubes will be slightly softer than carbon tubes. The predicted Young's modulus of BN tubes is 0.95 times the elastic modulus of carbon tubes, or of order 1 TPa.

17.4.2 Theoretical Predictions of BC_2N and BC_3

Due to the greater complexity of BC_2N, the unit cell is double that of graphite, and there are two possible arrangements of the B, C, and N atoms in the sheet, resulting in two different tube structures. Figure 17.11 shows the structure of tubes (Types I and II) of the same diameter but made from different isomers of the sheet material [6]. The Type I sheet has inversion symmetry (as does graphite) while the Type II sheet does not (similar to BN). Thus, it is not surprising that band structure calculations on the electrical properties of the Type I and Type II tubes parallel the properties of carbon and BN nanotubes, respectively. Type I tubes range from semiconducting to metallic depending on diameter and chirality, while the Type II tubes are predicted to be semiconducting independent of tube parameters. The most unique feature of tubes made from this material is that the arrangement of atoms (chain of conducting carbon alternating with a string of insulating BN) in the Type II tubule resembles a solenoid. Doping this semiconducting Type II tubule to metallicity

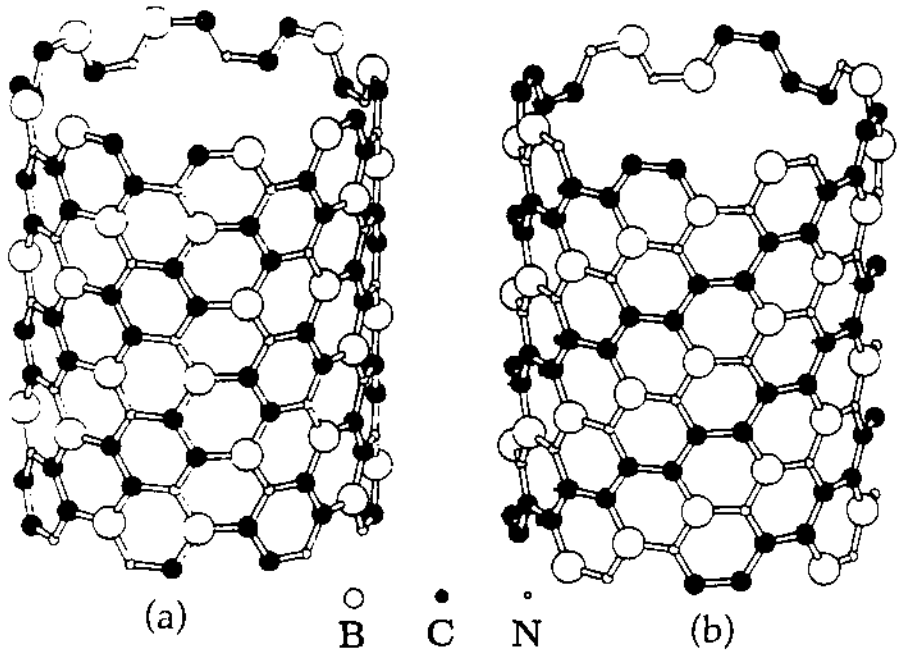

Figure 17.11 Theoretically determined tubules of isomers of BC_2N. These are the (4, 4) tubes in the indexing numerology of tubes. (Courtesy of Yoshiyuki Miyamoto.)

would cause the electrons to flow in a helical pattern along the chain of carbon atoms, becoming a *nanocoil*!

The electrical behavior of BC_3 tubes is rather complex, but the most significant result from the theoretical calculations predicts concentric tubes of BC_3 to be metallic [7]. Thus, all multiwalled structures made from this material are likely to be good conductors. On the other hand, single-wall, isolated BC_3 tubes are predicted to be semiconducting. Interestingly, when a number of such semiconducting tubes are aligned and brought into contact, the resulting bundle of tubes constitutes a metallic system.

17.5 SYNTHESIS OF BORON-NITRIDE-CONTAINING NANOTUBES

17.5.1 Synthesis of BN Nanotubes

The similarity between graphite and hexagonal BN suggests that some of the successful synthesis methods used for carbon nanotube production might be adapted to $B_xC_yN_z$ nanotube growth. This is indeed the case. A nonequilibrium plasma arc technique has been used to produce pure BN nanotubes [13]. To avoid the possibility of carbon contamination, no graphite components are used in this synthesis. The insulating nature of bulk BN prevents the use of a pure BN electrode. Instead, a pressed rod of hexagonal BN (white in color) is inserted into a hollow tungsten (W) electrode, forming a compound anode. The

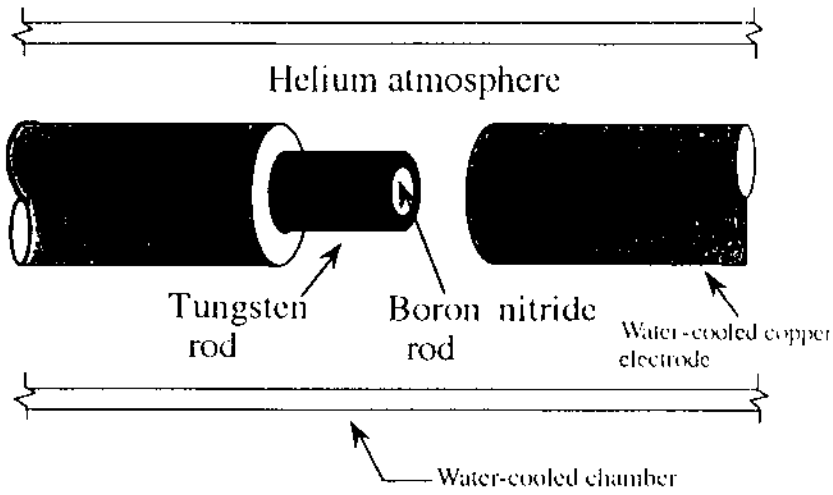

Figure 17.12 Electrode configuration used for the synthesis of BN nanotubes.

cathode consists of a rapidly cooled pure copper electrode (Fig. 17.12). During discharge the environmental helium gas is maintained at 650 torr and a dc current between 50 and 140 A is applied to maintain a constant potential drop of 30 volts between the electrodes while arcing.

Arcing the BN/W compound electrode results in a dark gray soot deposit on the copper cathode, in contrast to the cohesive cylindrical boule, which typically grows on the cathode upon graphite arcing. Due to instabilities, however, the BN/W arc burns only for a short time, thus yielding a limited quantity of soot. Pieces of solidified tungsten are often found spattered inside the chamber, indicating that the temperature at the anode during synthesis exceeds 3700 K, the melting point of tungsten. Other synthesis methods, using different catalysts, are also possible (see Section 17.7).

17.5.2 Characterization

17.5.2.1 High-Resolution TEM The preferred analytical tool for nanotube characterization is transmission electron microscopy (TEM).[2] Figure 17.13 shows a typical TEM image of the dark gray cathodic deposit produced in the arc-discharge chamber of a BN/W arc run. There are apparent numerous structures of distinct and contrasting morphologies. The large amorphous band covering nearly the entire lower half of the image is a portion of the support grid. The dark clusters scattered throughout the upper half of the image are tentatively identified as tungsten. Most importantly, Figure 17.13 clearly shows structures that appear to be multiwalled nanotubes, with inner (outer) diame-

[2] Cathodic deposit was characterized using a JEOL JEM 200CX TEM with 200 keV accelerating voltage.

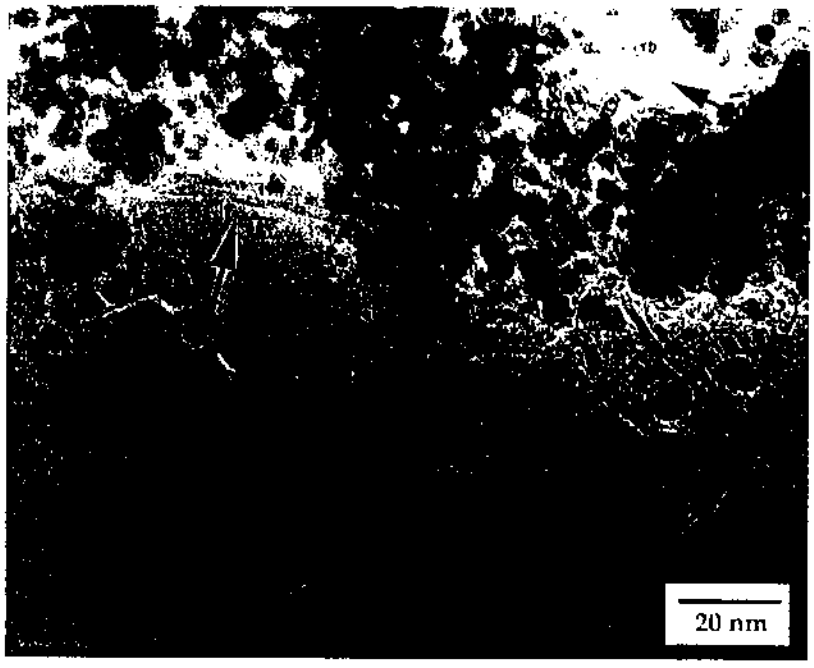

Figure 17.13 TEM image of soot produced in BN nanotube synthesis. Black arrows point out to sections of tubes. Big black arrows point to one long tube.

ters on the order of 1–3 nm (6–8 nm) and lengths exceeding 200 nm. The two dark arrows in Figure 17.13 identify one such tube, which extends beyond the left and right borders of the image. The light arrow in Figure 17.13 identifies another multiwalled tube of apparently shorter length.

Figure 17.14 shows a high-resolution TEM image of a portion of an observed nanotube. This and other similar images exhibit sharp lattice fringes, indicating that the walls of the tubes are well ordered with an interlayer distance of ~3.3 Å consistent with the interplanar distance of 3.33 Å in bulk hexagonal boron nitride [9]. The particular tube shown in Figure 17.14 has eight walls; similar tubes with wall numbers ranging from two to nine have been observed.

17.5.2.2 Electron Energy Loss Spectroscopy Although no graphite is used in the particular synthesis process described in detail above, confirmation of the chemical makeup and stoichiometry is crucial for conclusive evidence of BN nanotube discovery. Determination of the chemistry and stoichiometry of individual tubes is possible using electron energy loss spectroscopy (EELS) inside the TEM. High spatial resolution EELS studies have been performed [13] on portions of tubes suspended over holes in the carbon support grid as characterized in Figure 17.15. Figure 17.16 shows a characteristic tube energy loss spectrum, collected by probing a 10 nm region of the tube. Two distinct absorption features are revealed, one beginning at 188 eV and another at 401 eV. These correspond to the known *K*-edge onsets for boron and nitrogen, respec-

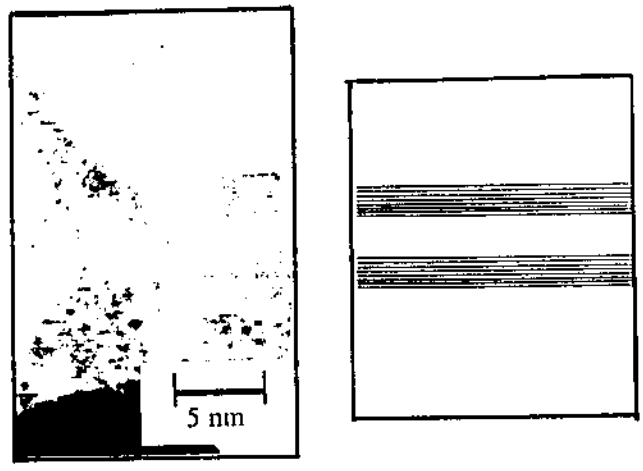

Figure 17.14 High-resolution TEM image of a multiwalled BN nanotube clearly showing the inner diameter and the equal number of lattice fringes on either side representing the number of tube walls. This tube has eight walls.

tively. The fine structure in the spectrum reveals the sp^2 bonding between boron and nitrogen [14]. Noteworthy is the absence of any feature at 284 eV, the *K*-edge absorption for carbon. Quantification of the tube EELS spectrum gives a B/N ratio of 1.14, consistent with a stoichiometry of BN (due to uncertainties in baseline corrections, the given B/N ratio has an estimated error of 20%).

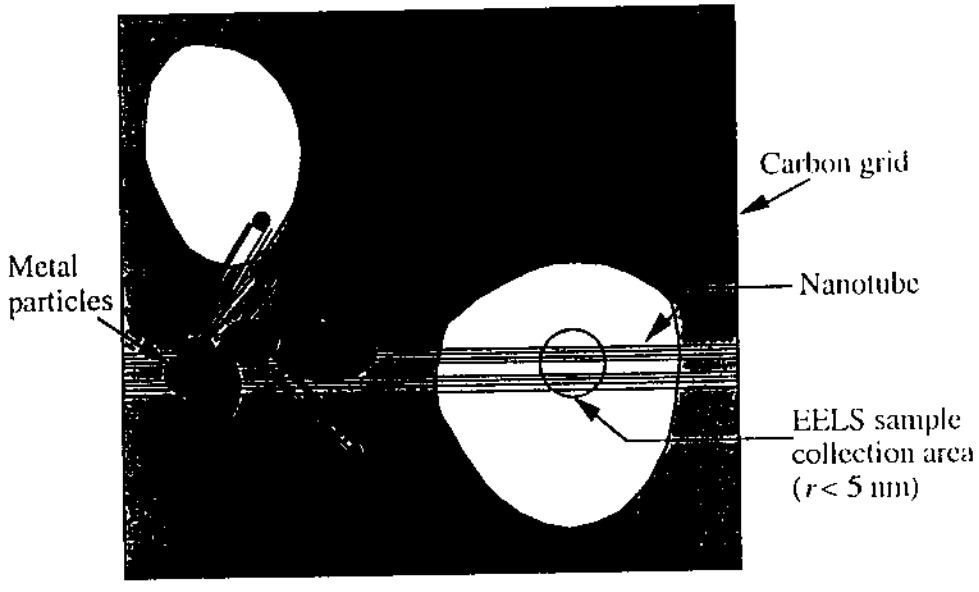

Figure 17.15 Schematic of configuration used in collecting the electron energy loss spectra on a nanotube.

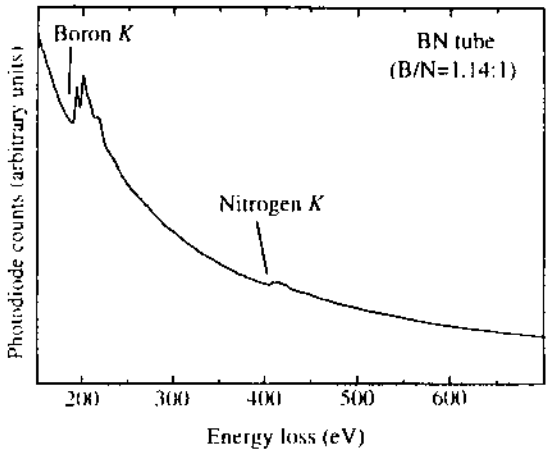

Figure 17.16 Electron energy loss spectrum of a BN nanotube confirming the sp^2 bonding of the boron and nitrogen and the absence of carbon in the tube structure. Quantitative analysis gives a B/N ratio of 1:1.14.

17.5.3 Possible Growth Scenario

A careful study of the ends of BN nanotubes synthesized using the tungsten electrode method reveals an interesting feature. As seen in Figure 17.17, the observed end contains a metal particle, most likely tungsten or a tungsten compound with boron and nitrogen. In contrast to the carbon nanotube, where the capping is fullerene-like or involves pentagons and heptagons, the BN tube closure by pentagon formation is suppressed due to the necessity of unfavorable B–B or N–N bonds. Nature seems to solve this problem by using, if available, a small metal cluster. The presence of many metal particles wrapped in layers of planar boron nitride, as is evident in Figure 17.13 and seen at higher magnifi-

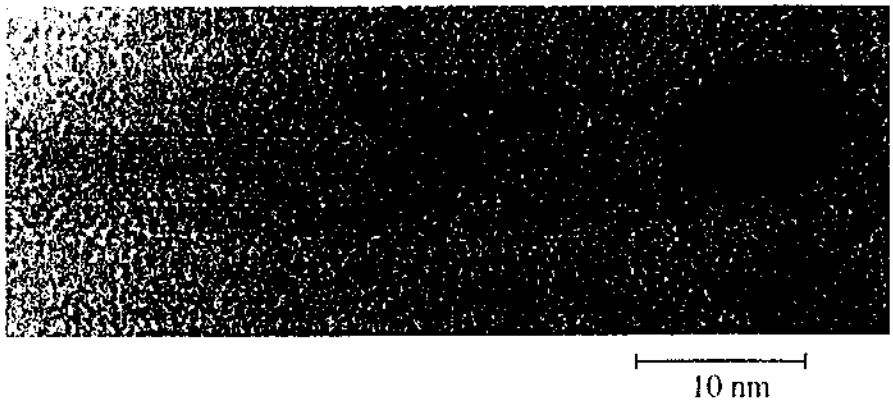

Figure 17.17 Micrograph of the end of a BN nanotube showing termination by a metal particle.

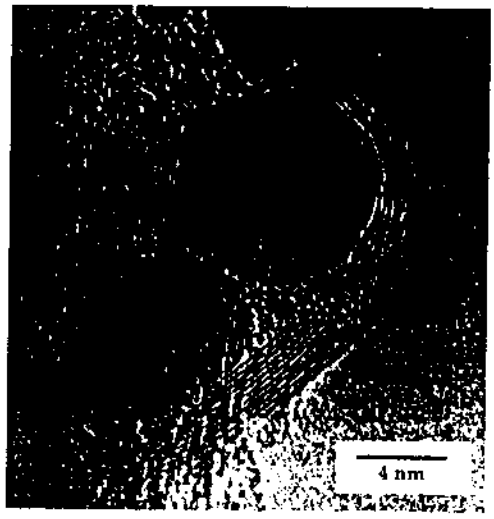

Figure 17.18 Micrograph of a metal particle covered with crystalline BN.

cation in Figure 17.18, suggests that in a high-curvature region of a covered particle, the outer layer of the BN coating may pull from the innermost layer (since the layer–layer interaction in BN is rather weak) and grow outward to form a nanotube. Given this scenario, the tube growth is likely to terminate when a metal particle collides with the open end of a growing tube and attaches to the dangling bonds, particularly if the metal forms stable nitrides and borides, as tungsten does.

Other experiments, using a slightly different arc-discharge synthesis configuration, have successfully produced single-walled BN nanotubes [15]. Tubes made by Loiseau et al. [15], however, do not have metal particles at the end, but terminate with flat tops, suggesting a square B–N arrangement at the ends compared to the hexagons in the wall. (Any even number polygon accommodates the preferred B–N bonding.)

17.5.4 Synthesis of BC_2N and BC_3

The synthesis of bulk (i.e., layered sheets of) BC_2N and BC_3 is achieved through the following chemical reactions:

$$CH_3CN + BCl_3 \xrightarrow{\sim 800\ ^\circ C} BC_2N + 3HCl$$

$$2BCl_3 + C_6H_6 \xrightarrow{\sim 800\ ^\circ C} 2BC_3 + 6HCl$$

Both BC_2N and BC_3 have bright metallic luster and resemble the layered structure of graphite due to the sp^2-like environment of each of the B, C, and N atoms in the bulk materials, signifying two-dimensionality. Resistivity measurements indicate that BC_2N is semiconducting with a gap of about 0.03 eV

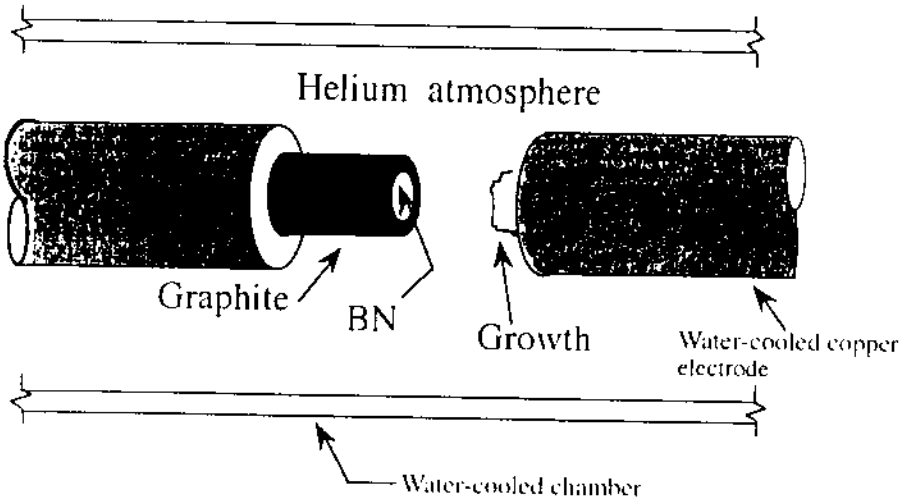

Figure 17.19 Schematic of the electrode configuration used to produce multiwalled BC_2N and BC_3 nanotubes in the arc-discharge chamber.

and BC_3 is semimetallic. The synthesis and characterization of both of these novel materials were done by Kouvetakis et al. in 1989 [16].

Along with the synthesis of carbon and BN nanotubes, the arc discharge allows for the successful production of tubes with other novel stoichiometries of boron, carbon, and nitrogen as well [17]. The arc configuration used in one experiment is described schematically in Figure 17.19. An insulating BN piece is inserted into a hollowed graphite rod resulting in a compound electrode. The cathode is the water-cooled copper piece as in the other experiments. The chamber parameters are similar to those used in multiwalled carbon nanotubes. The 450 torr helium pressure is bled into the chamber and the current is set to 55 A. Reminiscent of the carbon scenario, the compound BN/C electrode erodes and a growth occurs on the cooled copper surface. Detailed examination of the boule after arcing finds the inner core to be harder than the surrounding layers, which is in direct contrast to observations of pure carbon boule samples. However, in the case of a compound BN/C electrode, the central region contains hexagonal BN, a ceramic; therefore, from simple geometric arguments, a harder inner core is reasonable. The color of the boule, too, is gray instead of the typical carbon black, suggesting that the originally white BN has indeed been consumed in the arcing process and mixed with the black graphitic material. Figure 17.20 is a representative scanning electron micrograph (SEM) of the inner core boule material from this experiment. Tubes are clearly visible in the image along with significant quantities of bulk material. As is evident from Figure 17.20, the yield of nanotube structures is low in this experiment. TEM and EELS studies [17] confirm the crystallinity of the tube structure and individual tube stoichiometries of BC_2N and BC_3. In fact, EELS analysis also revealed that the sample contains nanotubes of pure carbon. Thus, using the configuration shown in Figure 17.19, the nonequilibrium arc-discharge tech-

Figure 17.20 SEM image of boule sample from a combined boron, carbon, and nitrogen experiment.

nique simultaneously produces multiwalled nanotubes of BC_2N, BC_3, and pure carbon.

Other studies using boron, carbon, and nitrogen have bound similar results [18–20].

17.6 ELASTIC PROPERTIES OF BN NANOTUBES

The elastic properties of an individual boron nitride (BN) nanotube have been experimentally determined through in situ studies in the transmission electron microscope [21]. These experiments are motivated by similar experiments on carbon nanotubes, first performed by Treacy et al. [22]. Analysis using the thermal vibration amplitude of a cantilevered BN nanotube yields a Young's modulus of 1.22 TPa. Because elastic measurements probe the microstructure of a material, the high value of the elastic constant suggests the BN nanotubes are indeed crystalline with few defects as observed in high-resolution micrographs.

Comparison with other materials finds BN nanotubes to be the stiffest insulating fiber known. Hexagonal BN is well known for its high-temperature resistance, and combined with these high-strength properties, BN nanotubes have the potential for unique applications in many different areas.

17.6.1 Vibrating BN Nanotube

Figure 17.21 is a TEM image of a BN nanotube specimen at 300 K. Two individual BN nanotubes are clearly visible, both cantilevered over a hole in the support grid. A short BN tube in the lower right region of the image (identified

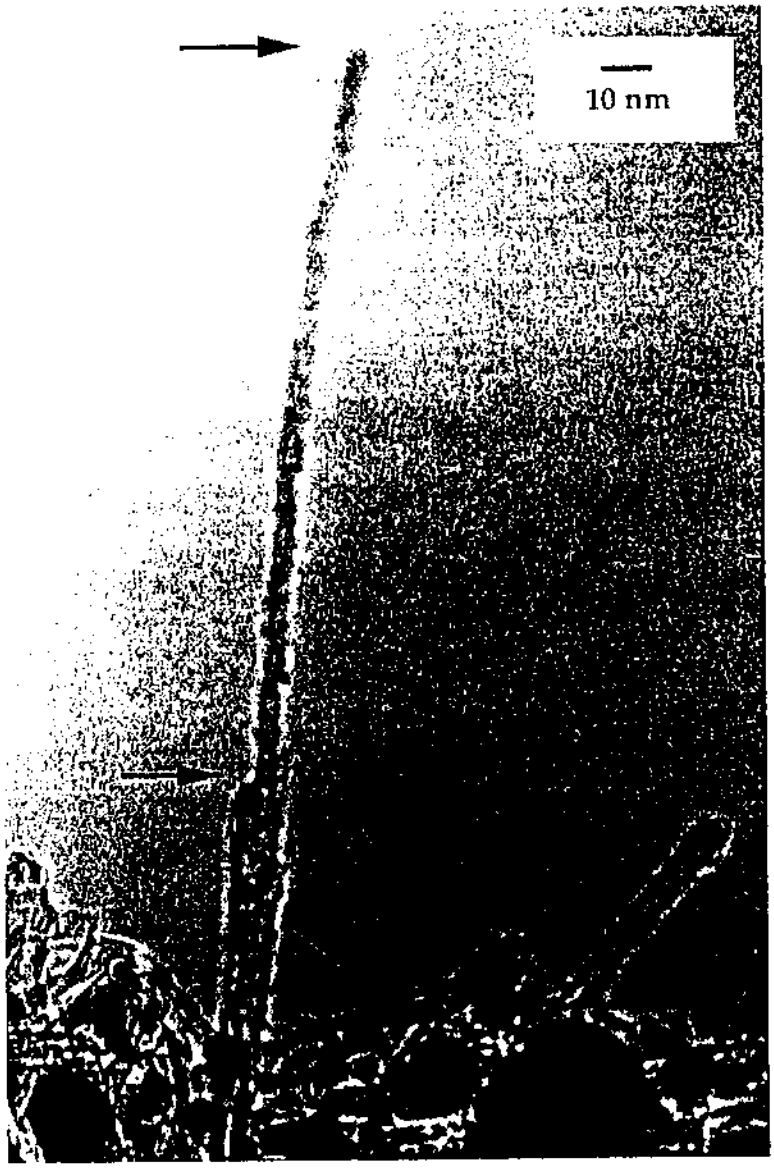

Figure 17.21 Vibrating BN nanotube at $T = 300$ K.

by a white arrow) has a clearly visible metal particle at its tip: the entirety of the tube is in clear focus, indicating a small vibration amplitude. The central region of Figure 17.21 shows a single long cantilevered BN nanotube. The base (lower black arrow) of this nanotube is in clear focus, while closer to the tip region (upper black arrow) the image becomes successively more blurred. Rotation studies verified that the blurring nature of the tip was not due to sample tilt, and variations in electron flux had no effect on the image, confirming that the tube vibration was due to thermal effects.

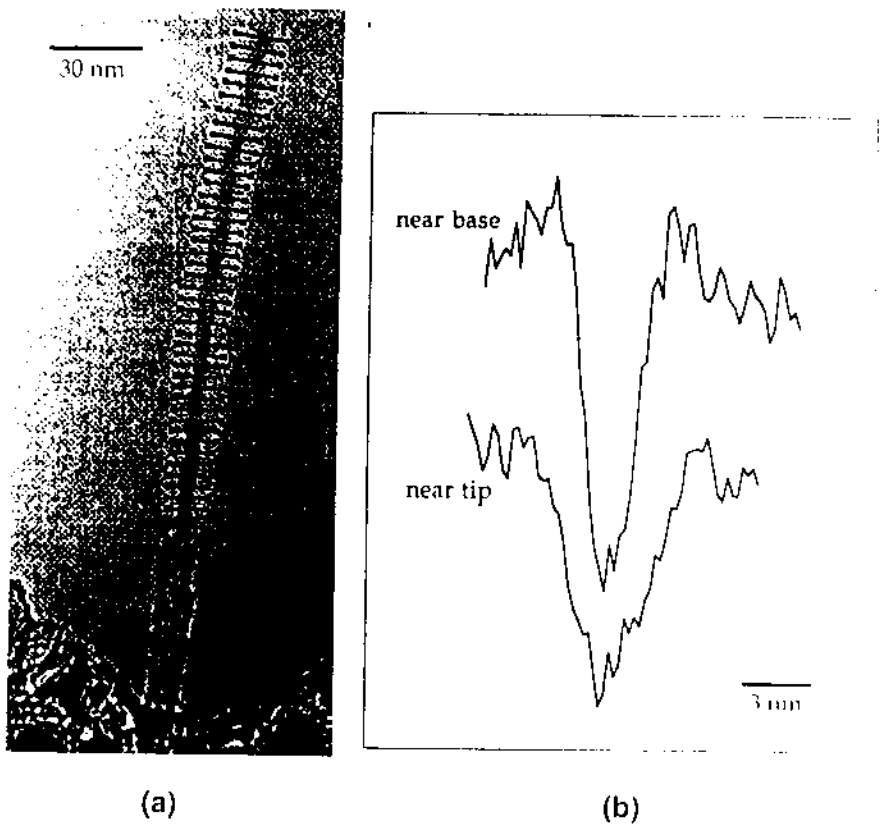

Figure 17.22 Line scan data of vibrating BN nanotube. (a) Placement of scans on the tube image. (b) Line scans near base and tip.

17.6.2 Data Analysis

To quantify the amplitudes of the vibration modes of the nanotube in the image plane, a series of intensity line scans perpendicular to the nanotube axis were performed on the micrograph of Figure 17.21. Figure 17.22a indicates the positions of the scans (short horizontal bars) while Figure 17.22b shows two representative intensity scans, one near the supported base and one near the nanotube tip. Because the tube extends out over unsupported area, the sudden drop from the background signifies the high contrast due to the tube. Near the supported base, the scan shows a sharper drop in contrast as compared to the line scan near the tip. This is consistent with the condition of focus at the base versus blurring at the end, which is depicted visually in Figure 17.21. From the width of the high-contrast region, the apparent tube diameter at points along the length of the structure is determined. As expected, the apparent tube width at the tip is greater than that at the base. The width of the nanotube at the base, where the vibration amplitude falls to zero, is 3.5 nm.

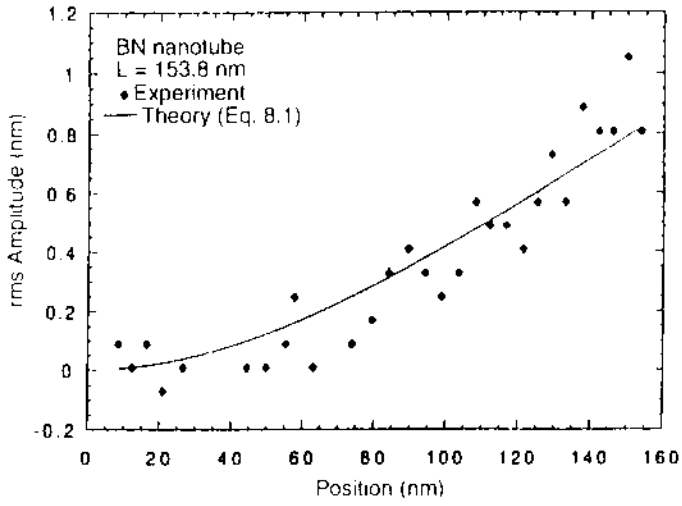

Figure 17.23 Plot of rms amplitude versus position for oscillating BN nanotube. Note general trend looks like the fundamental mode of a cantilever.

Figure 17.23 shows (as diamonds) the rms amplitude of the BN nanotube as a function of distance from the nanotube base, determined from a deconvolution of the intensity line scans from the baseline scan. As expected, the vibration amplitude increases with increasing distance from the clamped base of the nanotube.

17.6.3 Derivation of *Y* for a Thermally Excited Cantilever

The unique size of these nanotubes leads to interesting questions regarding the calculation of their mechanical properties. Can the tubes be treated as continuous hollow cylindrical structures or does their nanometer size call for a more discrete treatment? Doublet mechanics, a recently developed analytic approach to mechanics that incorporates the discrete nature of matter in the calculation of bulk behavior, has the potential to answer such a question [23]. Meanwhile, empirical potentials and first-principles total-energy calculations indicate that relationships derivable from continuum elasticity theory are applicable even for tubes with diameters as small as a C_{60} molecule (7 Å) [24].

The nanotube is approximated as a cantilever of length L, rigidly clamped at one end, freely vibrating at the other with a uniform circular cross section of outer diameter a and inner diameter b and mass per unit length μ. A schematic of the mechanical system is shown in Figure 17.24. Ideally a multiwalled tube is not a Bernoulli–Euler beam because the elastic property of the tube walls is, in fact, different from that of the area in-between, where the van der Waals force acts. However, the region that distinguishes the wall from the area in-between is so small that the error in assuming a multiwalled nanotube to be a uniform rigid beam is negligible. The displacement, $u(x, t)$, of the vibrating nanotube is

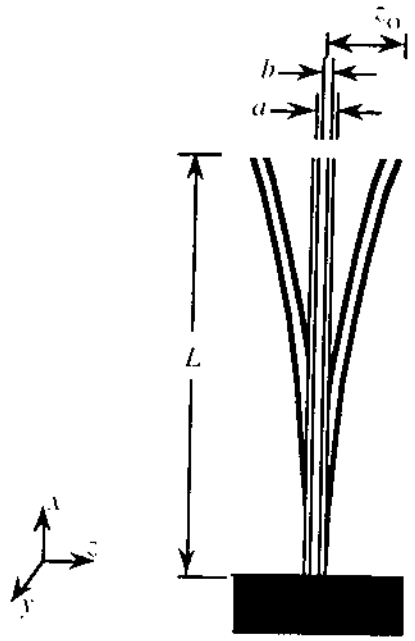

Figure 17.24 Schematic of mechanical system used to approximate a cantilevered nanotube.

a function of distance x and time t and can be described as a superposition of normal modes,

$$u(x,t) = \sum_{n=1}^{\infty} u_n(x,t) = z_0 \sum_{n=1}^{\infty} \alpha_n \phi_n(x) \sin \omega_n t \tag{17.2}$$

where z_0 is the maximum amplitude and α_n is the relative amplitude of the normal mode $\phi_n(x)$ at frequency ω_n. The complete set of normalized normal modes of a cantilever beam are

$$\phi_n(x) = \frac{1}{2}\left(\cosh \beta_n x - \cos \beta_n x - \frac{\cosh \beta_n L + \cos \beta_n L}{\sinh \beta_n L + \sin \beta_n L}(\sinh \beta_n x - \sin \beta_n x)\right) \tag{17.3}$$

with $\beta_n L = 1.8751, 4.6941, 7.8548$, and 10.996 for $n = 1, 2, 3$, and 4, respectively, and approximately $((2n-1)\pi)/2$ for $n > 4$. Young's modulus, Y, is embedded in the associated frequency expression,

$$\omega_n = (\beta_n L)^2 \sqrt{\frac{YI}{\mu L^4}} = (\beta_n L)^2 \sqrt{\frac{Y\pi(a^4 - b^4)}{64\mu L^4}} \tag{17.4}$$

where the second moment of area $I = (\pi(a^4 - b^4))/64$ is for a hollow circular cross section.

In order to extract a value for Y from the experimental data, let us consider the energy of the system. The average kinetic energy of a given mode is

$$\langle E_n^{\text{kinetic}} \rangle = \int_0^L \frac{1}{2}\mu \langle [\dot{u}_n(x,t)^2] \rangle \, dx = \frac{1}{2}\mu\omega_n^2 z_0^2 \alpha_n^2 \int_0^L [\phi_n(x)]^2 \, dx \langle \cos^2 \omega_n t \rangle \quad (17.5)$$

From the equipartition theorem, the average kinetic energy in each mode is $k_B T/2$, where k_B is Boltzmann's constant and T is the temperature. Equation Eq. (17.5) to $k_B T/2$ and using Eq. (17.4) yields

$$z_n = \sqrt{\frac{8k_B T}{\mu\omega_n^2 z_0^2 L}} \frac{1}{(\beta_n L)^2} \sqrt{\frac{512L^3 k_B T}{Y\pi(a^4 - b^4)z_0^2}} \quad (17.6)$$

Hence, Eq. (17.2) becomes

$$u(x,t) = \sqrt{\frac{512L^3 k_B T}{Y\pi(a^4 - b^4)}} \sum_{n=1}^{n_{\max}} \frac{1}{(\beta_n L)^2} \phi_n(x) \sin \omega_n t \quad (17.7)$$

Thus, the equipartition theorem fixes the relative amplitude of each mode. The amplitude contribution of higher modes falls off as $\propto (1/n^2)$; therefore, the vibration amplitude profile is dominated by the first few modes. The sum is ultimately limited at room temperature by $n_{\max} \approx 85$, where $\hbar\omega_{n_{\max}} \approx k_B T$.

The present formulation is an exact solution to the problem of a cantilever oscillating due to thermal effects. However, as stated earlier, the nanotube walls are treated as a single uniform material instead of discrete layers, a clear approximation.

17.6.4 Calculating Y_{BN}

The BN nanotube is approximated as a cantilevered Bernoulli–Euler beam of length L_{BN}, rigidly clamped at one end, freely vibrating at the other with a uniform circular cross section of outer diameter a_{BN} and inner diameter b_{BN}. Rewriting Eq. (17.7) for the displacement of a cantilevered tube oscillating at temperature T in terms of BN nanotube parameters gives

$$u_{BN}(x,t) = \sqrt{\frac{512L_{BN}^3 k_B T}{Y_{BN}\pi(a_{BN}^4 - b_{BN}^4)}} \left(\sum_{n=1}^{n_{\max}} \frac{1}{(\beta_n L_{BN})^2} \phi_n(x) \sin \omega_n t \right) \quad (17.8)$$

The markers in Figure 17.23 are the experimental data and the solid line is the fit using Eq. (17.8). From the fit, the maximum rms amplitude is found to be

0.8 nm. This fit together with the measured dimensions of the nanotube, $a_{BN} = 3.5$ nm, $b_{BN} = 2.2$ nm, and $L_{BN} = 153.8$ nm, yields an elastic modulus of $Y_{BN} = 1.22$ TPa for the BN nanotube at 300 K. Incorporating in the analysis the metal particle at the nanotube tip does not alter the result.

17.6.5 Discussion of Experimental Parameters for Y_{BN} Measurement

In the above calculation, the base of the cantilever has been taken to be where the single tube extends over the hole, as pointed to by the lower black arrow in Figure 17.21. (The focus condition supports this assumption since the region below the lower black arrow in Fig. 17.21 is entirely in focus.) If, instead, the point of rigid clamping is assumed to be directly at the clump, the mechanical system is then described by a beam with a varying second moment of area, $I = I(x)$. However, the second moment of area of the region where several tubes extend from the clump a short distance is much large than that of the single tube, and thus the combined system dynamically behaves as if the cantilevered tube was rigidly clamped at the position pointed out by the lower black arrow. Thus, the calculations for the combined system are identical to the mechanical system assumed in deriving Eq. (17.8), and the result for the elastic modulus of the BN nanotube is the same.

As mentioned previously, BN nanotubes synthesized by the tungsten-arc technique often terminate with a metal particle. If we assume there is a tungsten particle with a diameter on the order of the outer tube diameter and repeat the calculation, we find that the fundamental frequency goes down by 17% but the BN tube elastic modulus does not change. This is consistent with a simple mass–spring system, where the frequency depends on the mass and elastic constant of the spring, but the spring constant is independent of the mass as long as it is under its elastic limit.

17.6.6 Comparison of Elastic Moduli

Theoretically, the elastic modulus of a BN nanotube should be slightly smaller than that of a carbon nanotube. Although the structures are similar, the phonon frequencies [25] in graphite are calculated to be higher than those in planar BN, suggesting that the carbon–carbon bond is stronger than the boron–nitrogen bond. The experimental result for BN reflects this difference when compared to measured values of multiwalled carbon nanotubes [22].

The BN nanotube Young's modulus is 14 times greater than the measured in-plane modulus of bulk hexagonal BN material [33]. This difference is possibly due to the tube being a defect-free single crystalline piece, while the bulk hexagonal material is a composite of defected layers. Also, it is conceivable that the curvature of the tube strengthens the sp^2 bonding between the boron and nitrogen atoms, resulting in a material with improved mechanical properties. Thus, this experimental measurement shows the impressive change in elastic properties of a material due to nanometer scale sample geometry.

TABLE 17.1 Table of Elastic Moduli of a Variety of Fiber Materials

Material	Y (TPa)	Reference
Carbon fiber	0.2–0.8	26
Carbon nanotube	0.4–4	22
BN nanotube	1.22	21
Kevlar-49	0.112	27, p. II-2
E-glass fiber	0.074	28
SiC fiber	0.2	29
Steel wire	0.2	30
Copper wire	0.110	31
$Bi_2Sr_2Ca_1Cu_2O_x$ whisker	0.02	32
$Bi_2Sr_2Ca_2Cu_3O_x$ whisker	0.03	32

Indeed, fibers often have improved elastic properties in comparison to the bulk material [34]. Table 17.1 shows the Young's moduli of a range of fiber materials. The BN nanotube is an order of magnitude stiffer than any other insulating fiber and the second stiffest material after carbon nanotubes.

17.7 SUMMARY OF BN, BC_2N AND BC_3 NANOTUBE PROPERTIES AND OTHER $B_xC_yN_z$ STRUCTURES

The pure BN and carbon-containing sp^2-bonded host materials discussed in this chapter form the basis for a number of interesting structures. The synthesis and characterization of such $B_xC_yN_z$ materials represents an area of active experimental and theoretical research. Table 17.2 summarizes much of the theoretical and experimental work that has been presented here on nanotubes synthesized from boron, carbon, and nitrogen. From Table 17.2 it is evident that,

TABLE 17.2 Summary of Predicted and Measured Properties of $B_xC_yN_z$ Nanotubes

Type of Nanotube	Predicted Properties				Experimentally Determined	
	Electrical	E_{gap} (eV)	Y (TPa)	Y (TPa)	Single-Walled Nanotube Found?	
Carbon	Semiconducting or metallic	0–1.5	1.2	1.35	Yes	
BN	Semiconducting	4–5.5	0.95–0.65	1.18	Yes	
BC_2N I	Semiconducting or metallic				No	
BC_2N II	Semiconducting	1.28			No	
BC_3	Metallic				No	

so far, the largest amount of work, both theoretcial and experimental, has been done on carbon and BN nanotubes. Clearly, minimal experimental work has been done on BC_2N and BC_3. Carbon nanotubes have existed for the longest period of time and large quantities of tube material are readily available due to the stable arcing of graphite, which produces the plentiful tube-containing boule. BN nanotubes, due to their potentially interesting electrical application, have also been studied, although techniques for large-scale production need to be explored.

Loiseau et al. [15] have used an arc-discharge method employing HfB$_2$ electrodes in a nitrogen atmosphere to synthesize BN nanotubes with wall number ranging from many to one. In this synthesis method, the Hf is apparently not incorporated into the tube itself, but rather acts as a catalyzing agent. The source of nitrogen for tube growth is from the N_2 environmental gas. The ends of the BN nanotubes so produced have flat layers perpendicular to the tube axis and are representative of the bond frustration that occurs upon tube closure (the simple six pentagon addition, which so beautifully closes a pure carbon nanotube, is not realized in BN nanotubes because the B–B bond is not favored).

Tantalum has also been used as the catalyzing agent in the synthesis of various nanoscale BN structures using arc-vaporization methods [19]. Pure BN nanotubes are produced, along with other nanoparticles including onion-like spheres similar to those produced by Banhart et al. [35] using high-intensity electron irradiation. In the study of Terrones et al. [19], circumstantial evidence is found for the presence of B_2N_2 squares at the BN nanotube tips, as well as B_3N_3 hexagons in the main fabric of the nanotubes.

Perhaps one of the most intriguing new developments in BN tube synthesis is the realization of nanotubes with segregated tube-wall stoichiometry. For example, Suenaga et al. [36] have produced multiwalled nanotubes containing pure carbon walls adjacent to pure BN walls, forming a sort of nanotube coaxial cable. In one specific tube studied carefully by electron energy loss spectroscopy, the innermost three walls of the tube contained only carbon, the next six walls were comprised of BN, and the last five outermost walls were again pure carbon. The entire 14-walled composite nanotube was 12 nm in diameter. Similar layer segregation is obtained for onion-like coverings over nanoparticles (quite often the core nanoparticle is composed of the catalyst material). The results of Suenaga and co-workers are consistent with the earlier findings of Redlich et al. [37], who observed B–C–N nanotubes consisting of concentric cylinders of BC_2N and pure carbon.

More recently, Zhang et al. [38] have used a reactive laser ablation method to synthesize multi-element nanotubes containing BN. The nanotubes contain a silicon carbide core followed by an amorphous silicon oxide intermediate layer; this composite nanorod is then sheathed with BN and carbon nanotube layers, segregated in the radial direction. It has been speculated that merging BN and carbon nanotube structures may be the basis for novel electronic device architectures.

ACKNOWLEDGMENTS

We thank the following people for helpful interactions: L. Benedict, K. Cherrey, M. L. Cohen, P. Collins, V. Crespi, R. Gronsky, S. G. Louie, R. Luyken, Y. Miyamoto, M. O'Keefe, A. Rubio, and Z. Weng-Sieh. This work was supported in part by the sp^2 Materials Initiative, Office of Energy Research, Office of Basic Energy Sciences, Materials Sciences Division of the U.S. Department of Energy under Contract No. DE-AC03-76SF00098.

REFERENCES

1. S. Iijima, *Nature* **1991**, *354*, 56–58.
2. H. W. Kroto, J. R. Heath, S. C. O'Brien, R. F. Curl, and R. E. Smalley, *Nature* **1985**, *318*, 162–163.
3. N. Hamada, S. Sawada, and A. Oshiyama, *Phys. Rev. Lett.* **1992**, *68*, 1579–1581.
4. G. Overney, W. Zhong, and D. Tománek, *Z. Phys. D* **1993**, *27*, 93–96.
5. A. Rubio, J. L. Corkill, and M. L. Cohen, *Phys. Rev. B* **1994**, *49*, 5081–5084.
6. Y. Miyamoto, A. Rubio,M. L. Cohen, and S. G. Louie, *Phys. Rev. B* **1994**, *50*, 4976–4979.
7. Y. Miyamoto, A. Rubio, M. L. Cohen, and S. G. Louie, *Phys. Rev. B* **1994**, *50*, 18360–18364.
8. M. S. Dresselhaus, G. Dresselhaus, and R. Saito, *Carbon* **1995**, *33*, 883–891.
9. R. S. Pease, *Acta Crystallogr.* **1952**, *5*, 356.
10. J. Kouvetakis, R. B. Kaner, M. L. Sattler, and N. Bartlett, *J. Chem. Soc. Chem. Commun.* **1986**, 1758.
11. X. Blase, A. Rubio, S. G. Louie, and M. L. Cohen, *Europhys. Lett.* **1994**, *28*, 335–340.
12. A. Zunger, A. Katzir, and A. Halperin, *Phys. Rev. B* **1976**, *13*, 5560–5573.
13. N. G. Chopra, R. J. Luyken, K. Cherrey, V. H. Crespi, M. L. Cohen, S. G. Louie, and A. Zettl, *Science* **1995**, *269*, 966–967.
14. L. Reimer, *Transmission Electron Microscopy*, P. W. Hawkes (ed.), Springer Series in Optical Sciences, Vol. 36, Springer-Verlag, Berlin, 1993.
15. A. Loiseau, F. Williame, N. Demoncy, G. Hug, and H. Pascard, *Phys. Rev. Lett.* **1996**, *76*, 4737–4740.
16. J. Kouvetakis, T. Sasaki, C. Chen, R. Hagiwara, M. Lerner, K. M. Krishnan, and N. Bartlett, *Synthetic Materials* **1989**, *34*, 1–7.
17. Z. Weng-Sieh, K. Cherrey, N. G. Chopra, X. Blase, Y. Miyamoto, A. Rubio, M. L. Cohen, S. G. Louie, A. Zettl, and R. Gronsky, *Phys. Rev. B* **1995**, *51*, 11229–11232.
18. O. Stephan, P. M. Ajayan, C. Colliex, Ph. Redlich, J. M. Lambert, P. Bernier, and P. Lefin, *Science* **1994**, *266*, 1683–1685.
19. M. Terrones, A. M. Benito, C. Manteca-Diego, W. K. Hsu, O. I. Osman, J. P. Hare, D. G. Reid, H. Terrones, A. K. Cheetham, K. Prassides, H. W. Kroto, and D. R. M. Walton, *Chem. Phys. Lett.* **1996**, *257*, 576–582.

20. Ph. Redlich, J. Loeffler, P. M. Ajayan, J. Bill, F. Aldinger, and M. Rühle, *Chem. Phys. Lett.* **1996**, *260*, 465–470.
21. N. G. Chopra and A. Zettl, *Solid State Commun.* **1998**, *105*, 297–300.
22. M. M. J. Treacy, T. W. Ebbesen, and J. M. Gibson, *Nature* **1996**, *381*, 678–680.
23. M. Ferrari, V. T. Granik, A. Imam, and J. C. Nadeau (eds.), *Advances in Doublet Mechanics*, Lecture Notes in Physics, Monogram Vol. 45, Springer-Verlag, Berlin, 1997.
24. D. H. Robertson, D. H. Brenner, and J. W. Mintmire, *Phys. Rev. B* **1992**, *45*, 12592–12595.
25. Y. Miyamoto, M. L. Cohen, and S. G. Louie, *Phys. Rev. B* **1995**, *52*, 14971–14975.
26. R. L. Jacobsen, T. M. Tritt, J. R. Guth, A. C. Ehrlich, and D. J. Gillespie, *Carbon* **1995**, *33*, 1217–1221.
27. DuPont, *Kevlar Aramid Fiber*, DuPont Advanced Fibers Systems, Wilmington, DE, 1992.
28. C. Matotzke, *Composites Sci. Technol.* **1994**, *50*, 393–405.
29. M. W. Barsoum, P. Kangutkar, and A. S. D. Wang, *Composites Sci. Technol.* **1992**, *44*, 257–269.
30. E. P. Popov, *Engineering Mechanics of Solids*, Prentice Hall, New York, 1990.
31. C.-L. Tsai and I. M. Daniel, *Composites Sci. Technol.* **1994**, *50*, 7–12.
32. T. M. Tritt, M. Marone, A. C. Ehrlich, M. J. Skove, D. J. Gillespie, R. L. Jacobsen, G. X. Tessema, J. P. Franck, and J. Jung, *Phys. Rev. Lett.* **1992**, *68*, 2531–2534.
33. Data supplied by Carborundum Corporation, Latrobe, PA.
34. X. Peters, *Composites* **1995**, *26*, 108–114.
35. F. Banhart, T. Fuller, P. Redlich, P. M. Ajayan et al., *Chem. Phys. Lett.* **1997**, *269*, 349–355.
36. K. Suenaga, C. Carbon, N. Demoncy, A. Loiseau et al., *Science* **1997**, *278*, 653–655.
37. Ph. Redlich, J. Loeffler, P. M. Ajayan et al., *Chem. Phys. Lett.* **1996**, *260*, 465–470.
38. Y. Zhang, K. Suenaga, and S. Iijima, *Science* **1998**, *281*, 973–975.